Ab initio high-pressure phase diagrams of Al-Mg alloys in the low solute concentration limit

Shambhu Bhandari Sharma,[1,*] Shailesh Mehta,[2] and Dario Alfè[1,3,4]

[1]*Department of Earth Sciences, University College London, Gower Street, London WC1E 6BT, United Kingdom*
[2]*AWE Nuclear Security Technologies, Aldermaston, Reading, Berkshire RG7 4PR, United Kingdom*
[3]*London Centre for Nanotechnology, University College London, London WC1E 6BT, United Kingdom*
[4]*Dipartimento di Fisica Ettore Pancini, Università di Napoli Federico II, Monte S. Angelo, Napoli I-80126, Italy*

(Received 2 July 2026; revised 30 September 2026; accepted 28 October 2026; published 16 November 2026)

Binary alloy phase diagrams at high pressure are essential for understanding solidification and chemical partitioning in both engineered materials and planetary interiors, yet their experimental determination becomes increasingly challenging under extreme conditions. We apply a fully *ab initio* approach [Sharma *et al.*, J. Chem. Phys. **162**, 184502 (2025)], based on density-functional theory, to compute the dilute-limit phase diagram of the Al–Mg system from ambient conditions up to 150 GPa. As a first step, we calculate the melting curves of pure fcc Al and pure hcp/bcc Mg, including the hcp–bcc phase boundary and triple point of Mg, all of which agree closely with available experimental data. The binary phase diagram is then constructed at both compositional extremes. On the Al-rich side, Mg consistently favors the liquid throughout the entire pressure range, with this preference strengthening monotonically under compression. On the Mg-rich side, Al partitions preferentially into the liquid at ambient pressure but undergoes a complete reversal within the bcc stability field of the Mg host, becoming solidfavoring ($k = 1.12 \pm 0.03$) by 60 GPa. This pressure-driven reversal inverts the topology of the Mg-rich coexistence field from a conventional downward-sloping to an upward-sloping phase boundary, and can be useful for models of planetary differentiation and interior chemical stratification.

DOI: 10.1103/q4q1-q4g8

I. INTRODUCTION

Phase diagrams map the equilibrium stability of competing phases as functions of temperature, pressure, and composition, and are the primary thermodynamic guide for understanding solidification, partitioning, and chemical evolution of materials. Even the simplest isomorphous binary metallic phase diagram already comprises distinct phase fields, including single-phase liquid and solid-solution regions and two-phase coexistence regions bounded by the solidus and liquidus. The solidus and liquidus boundaries, together with the solute partition coefficient, govern macrosegregation during solidification and the precipitation and dissolution of secondary phases during heat treatment during processing of alloys [1,2]. In planetary science, the same thermodynamic framework, extended to high pressure, determines how elements fractionate between solid and liquid phases during core solidification and mantle crystallisation, controlling the long-term chemical stratification of planetary interiors [1,2]. Phase diagrams are therefore the fundamental thermodynamic tool across materials science, metallurgy, and geoscience [3,4].

Phase diagram determination has been pursued by a broad spectrum of approaches. Classical experimental methods, including equilibrated-alloy analysis, diffusion couples, and thermal analysis techniques such as differential scanning calorimetry, are most effective at ambient or moderate pressures [5,6]. The CALPHAD approach fits parametric Gibbs energy models to experimental and computational data and extrapolates efficiently to multicomponent systems [7,8], but its databases are constructed almost exclusively from low-pressure data, making extrapolation to extreme conditions unreliable when experimental input is absent. Machine-learning methods, either as classifiers/regressors trained on thermodynamic databases or as interatomic potential surrogates for density-functional theory (DFT), offer high-throughput screening across composition space [9–11], though their reliability depends critically on training data coverage. First-principles free-energy methods evaluate phase boundaries directly from electronic-structure calculations without empirical fitting and are uniquely capable of accessing thermodynamic conditions beyond experimental reach. For solid-state boundaries, cluster-expansion methods combined with Monte Carlo sampling have been applied widely [12,13]. For solid–liquid alloy equilibria, the chemical potential and partitioning of a dilute solute in solid and liquid phases can be evaluated using thermodynamic integration, even up to Earth's core conditions [14,15].

Many binary systems phase diagrams of physical and technological importance involve one component present only at low concentration, defining the dilute-solute regime [14,16–18]. In this limit, the thermodynamic description simplifies

*Contact author: shambhu.sharma.22@ucl.ac.uk

Published by the American Physical Society under the terms of the Creative Commons Attribution 4.0 International license. Further distribution of this work must maintain attribution to the author(s) and the published article's title, journal citation, and DOI.

considerably: the solute chemical potential varies linearly with concentration, so the solidus and liquidus are fully determined by the excess chemical potential of the solute in each phase, a quantity that can be computed from first principles via thermodynamic integration and is formally exact at zero concentration [14,15]. In a recent paper [19], we developed and validated a general *ab initio* framework for computing binary alloy phase diagrams in this limit, applicable to binary alloys across wide pressure and temperature ranges, subject to the conditions that the dilute-solution and weak-perturbation approximations remain valid.

The Al–Mg system is of direct relevance to lightweight structural alloy design [20,21] and, at high pressures, serves as a well-defined model binary system for exploring high-pressure partitioning phenomena relevant to deep planetary interiors. Despite its physical importance, the high-pressure binary phase diagram of Al–Mg has not previously been determined from first principles across a wide pressure range; experimentally, binary phase boundaries are well characterized only at ambient pressure [22]. Here we apply the framework of Ref. [19] to the Al–Mg system from ambient conditions up to 150 GPa, establishing the *ab initio* melting curves of pure Al and Mg, the hcp–bcc solid-state transition and triple point of Mg, and the dilute-limit phase boundary at both compositional extremes.

II. METHODOLOGY

The theoretical framework used in this work is described in full detail in Ref. [19]; here we summarize the computational approach and the key thermodynamic relations for computing binary alloy phase diagrams in the dilute-solute limit. The framework proceeds in two stages. In the first, the melting curve of the pure solvent is established via the phase coexistence with free-energy correction (PCFC) approach. In the second, the solute excess chemical potential difference between the solid and liquid phases is computed via the chemical potential difference of solute (CPDS) approach. These quantities are then combined through dilute-solution phase-equilibrium relations to construct the solidus and liquidus of the binary alloy. The full workflow is illustrated in Fig. 1.

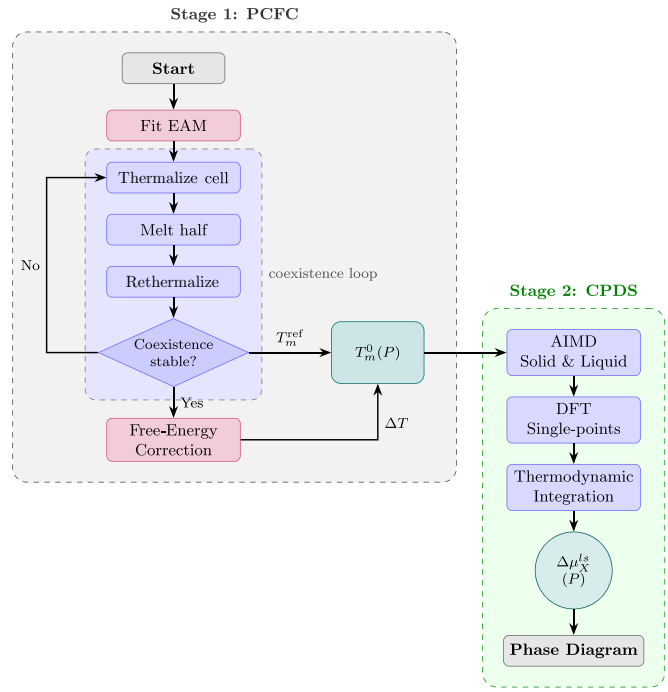


FIG. 1. Computational workflow for computing the *ab initio* binary alloy phase diagram in the dilute-solute limit. Stage 1 (PCFC) establishes the pure-solvent melting curve $T_m^0(P)$ via large-scale coexistence simulations and free-energy correction to DFT accuracy. Stage 2 (CPDS) computes the solute excess chemical potential difference $\Delta\mu_X^{ls}(P)$ via *ab initio* molecular dynamics and perturbative thermodynamic integration. The two outputs are combined through dilute-solution thermodynamic relations to construct the solidus and liquidus.

A. Pure-solvent melting curve: PCFC

The melting curve of each pure elemental component (Al, Mg) is established using the PCFC approach. Elemental reference potentials based on the embedded-atom method (EAM) [23] are parameterized to DFT energies and pressures from AIMD trajectories of the pure solid and liquid phases and are not used as binary alloy potentials. Since any EAM potential trained at a given pressure degrades in transferability when applied far from its training conditions, a multipotential strategy is adopted: two independent EAM potentials are trained per crystal structure at distinct pressures and applied within their respective regimes. Details of the reference potential parametrization, cutoff, and validation are provided in Sec. S1 of the Supplemental Material [24].

The reference potential drives large-scale classical molecular dynamics coexistence simulations, in which a simulation cell is prepared with solid and liquid regions in contact, and evolved in the microcanonical (NVE) ensemble until a stationary solid–liquid interface is established. The time-averaged temperature and pressure of this stationary state define the reference melting point $(P, T_m^{\rm ref})$, with statistical uncertainties estimated from a reblocking analysis [25].

The reference melting temperature is then corrected to DFT accuracy via a perturbative expansion of the Gibbs free energy difference between the DFT and EAM Hamiltonians. To first order, the temperature shift $\Delta T = T_m^{\rm DFT} - T_m^{\rm ref}$,

$$\Delta T \approx \frac{\Delta G^{ls}(T_m^{\rm ref})}{S^{ls}_{\rm ref}}, \tag{1}$$

where $S^{ls}_{\rm ref}$ is the entropy of fusion of the reference system, and $\Delta G^{ls} = \Delta G^{l} - \Delta G^{s}$ is the liquid–solid difference in the Gibbs free energy correction. The Helmholtz free energy difference between the two Hamiltonians is first evaluated perturbatively from DFT single-point energies on configurations sampled from the EAM ensemble,

$$\Delta F \approx \langle \Delta U \rangle_{\rm ref} - \frac{\langle \delta \Delta U^2 \rangle_{\rm ref}}{2 k_{\rm B} T}, \tag{2}$$

where $\Delta U = U_{\rm DFT} - U_{\rm ref}$ and $\delta \Delta U = \Delta U - \langle \Delta U \rangle_{\rm ref}$. The Gibbs free energy correction is then obtained by incorporating

the induced pressure change $\Delta p = p_{\mathrm{DFT}} - p_{\mathrm{ref}}$,

$$\Delta G \approx \Delta F - \frac{V \Delta p^2}{2K_T}, \tag{3}$$

where K_T is the isothermal bulk modulus [26], evaluated analytically for each phase from a third-order Birch–Murnaghan equation of state fitted to the reference-system $P - V$ isotherms.

B. Solid-state phase transition

When a pure component undergoes a pressure-induced structural transition, the stable solid phase at each pressure must be identified before the melting curve can be constructed, since it determines which crystal structure serves as the host lattice in the subsequent CPDS calculations. The stable phase at any (P, T) is the one with the lowest Gibbs free energy, and the phase boundary is located by the condition $G_\alpha(P, T) = G_\beta(P, T)$. Following Mehta *et al.* [27], the Gibbs free energy of each competing structure is computed from DFT within the quasiharmonic approximation [28], with the electronic contribution parametrised by a Birch–Murnaghan equation of state and the ionic contribution by an effective Einstein model. Solving the equal-free-energy condition numerically yields the transition pressure and traces the full phase boundary.

C. Solute chemical potential and phase diagram: CPDS

The central quantity for constructing the binary phase diagram in the dilute-solute limit is the excess chemical potential difference $\Delta\mu_X^{ls} = \mu_X^{\dagger l} - \mu_X^{\dagger s}$, which fully determines both the solute partition coefficient and the solidus and liquidus boundaries. In the limit of vanishing solute concentration $c_X \to 0$, the solute chemical potential takes the form [14,15]

$$\mu_X = k_{\mathrm{B}} T \ln c_X + \mu_X^{\dagger} + \mathcal{O}(c_X), \tag{4}$$

where $\mu_X^{\dagger}$ is the excess chemical potential in the limit of zero concentration. Imposing solid–liquid coexistence, $\mu_X^s = \mu_X^l$, yields to leading order the partition coefficient

$$k = \frac{c_X^s}{c_X^l} = \exp\left[\frac{\Delta\mu_X^{ls}}{k_{\mathrm{B}} T_m}\right]. \tag{5}$$

The shift in melting temperature with solute concentration, relative to the pure-solvent value $T_m^0 \equiv T_m^{\mathrm{DFT}}$, defines the liquidus and solidus curves:

$$T_m^l = T_m^0 + \frac{k_{\mathrm{B}} T_m^l}{\Delta s_A^0}\left(e^{\Delta\mu_X^{ls}/k_{\mathrm{B}} T_m^l} - 1\right) c_X^l, \tag{6}$$

$$T_m^s = T_m^0 + \frac{k_{\mathrm{B}} T_m^s}{\Delta s_A^0}\left(1 - e^{-\Delta\mu_X^{ls}/k_{\mathrm{B}} T_m^s}\right) c_X^s, \tag{7}$$

where $T_m^0(P)$ and $\Delta s_A^0(P)$ are the pure-solvent melting temperature and entropy of fusion. Equations (6) and (7) constitute the central governing relations of the entire framework: Determining the binary phase diagram reduces to evaluating $T_m^0(P)$, $\Delta s_A^0(P)$, and $\Delta\mu_X^{ls}(P)$ at each pressure, for which all subsequent calculations in Secs. III A and III B are performed. The entropy of fusion per atom is evaluated from solid and liquid trajectories at coexistence conditions (P, T_m^0):

$$\Delta s_A^0(P) = \frac{E^l - E^s + P(V^l - V^s)}{T_m^0(P)},$$

where E^l, E^s and V^l, V^s are the energies and atomic volumes of the liquid and solid phases. Equations (6) and (7) are solved self-consistently at each pressure to yield the phase diagram over the composition range in which the dilute approximation remains valid. Full details of the statistical uncertainty propagation to k and the phase boundary corridors are given in Sec. S6 of the Supplemental Material [24].

D. Computing $\Delta\mu_X^{ls}$ via thermodynamic integration

The excess chemical potential difference is computed by coupling the pure-solvent system ($\lambda = 0$) to the single-solute-substituted system ($\lambda = 1$) through the hybrid Hamiltonian $U_\lambda = (1 - \lambda)U_0 + \lambda U_1$. The exact Helmholtz free energy difference between the two endpoints is

$$\Delta F = F_1 - F_0 = \int_0^1 \langle U_1 - U_0 \rangle_\lambda \, \mathrm{d}\lambda, \tag{8}$$

where $\langle \cdots \rangle_\lambda$ denotes the thermal average under U_λ [14]. When $U_1 - U_0$ is a weak perturbation, satisfied here since a single solute substitution induces only a localized perturbation of the host, the integrand $\langle \Delta U \rangle_\lambda$ is well approximated as linear in λ, and the integral reduces to a perturbative two-endpoint scheme. Applying second-order perturbation theory at each endpoint,

$$\Delta F \approx \langle \Delta U \rangle_{\lambda=0} - \frac{\langle \delta\Delta U^2 \rangle_{\lambda=0}}{2k_{\mathrm{B}} T}, \tag{9}$$

$$\Delta F \approx \langle \Delta U \rangle_{\lambda=1} + \frac{\langle \delta\Delta U^2 \rangle_{\lambda=1}}{2k_{\mathrm{B}} T}, \tag{10}$$

where $\delta\Delta U = \Delta U - \langle \Delta U \rangle_\lambda$ is the fluctuation of the energy difference about its mean. The two estimates in Eqs. (9) and (10) are combined using a piecewise-linear estimator: When the linear approximations anchored at $\lambda = 0$ and $\lambda = 1$ do not intersect within [0,1], the integrand is effectively linear and the simple average $\bar{U} = \frac{1}{2}(\langle \Delta U \rangle_0 + \langle \Delta U \rangle_1)$ is adopted; when they intersect at an interior point $\lambda^* \in (0, 1)$, indicating curvature in the integrand, the piecewise-linear estimator is applied, integrating each linear approximation over its respective domain $[0, \lambda^*]$ and $[\lambda^*, 1]$.

The chemical potential difference then follows directly as $\Delta\mu_X^{ls} = \Delta F^l - \Delta F^s$, where ΔF^l and ΔF^s are computed independently for the liquid and solid phases.

E. Implementation

AIMD simulations in the canonical (NVT) ensemble are performed independently for both solid and liquid phases at each (P, T_m^0) state point, using two distinct systems: the pure solvent A ($\lambda = 0$) and the system in which one solvent atom is replaced by the solute X ($\lambda = 1$). At each λ endpoint and for each phase, statistically independent configurations are extracted from the AIMD trajectory. For each extracted configuration, two DFT single-point energy evaluations are performed: For configurations sampled from the $\lambda = 0$ trajectory, the energy U_0 is computed for the pure-solvent

configuration and then U_1 is computed after substituting one solvent atom with the solute; for configurations sampled from the $\lambda = 1$ trajectory, the procedure is reversed, computing U_1 for the solute-containing configuration and U_0 after replacing the solute with a solvent atom. This cross evaluation at both endpoints is essential for computing both $\langle \Delta U \rangle_\lambda$ and $\langle \delta \Delta U^2 \rangle_\lambda$ at each endpoint independently, without requiring any intermediate λ simulations.

F. Computational details

All DFT and AIMD calculations are performed using the VIENNA *AB INITIO* SIMULATION PACKAGE [29,30] with the projector-augmented-wave (PAW) method [31] and the Perdew–Burke–Ernzerhof generalized gradient approximation [32]. The PAW core radii for Al and Mg are 1.01 Å and 1.06 Å, respectively, and a plane-wave cutoff energy of 312 eV is used throughout with `PREC = Accurate`, confirmed to be sufficiently converged by tests up to 400 eV. Finite-temperature electronic effects are treated within the Mermin formalism [33], and constant-temperature AIMD simulations employ a Nosé thermostat [34]. Brillouin-zone sampling uses Monkhorst–Pack grids [35], with mesh densities converged individually for each stage of the calculation. For the DFT single-point energy evaluations in the thermodynamic integration (CPDS stage), Monkhorst–Pack k-point grids up to $6 \times 6 \times 6$ are used, reduced to the irreducible Brillouin zone of the underlying crystal structure (cubic for fcc Al and bcc Mg; hexagonal for hcp Mg), which significantly improves computational efficiency compared with full nonsymmetric grids. Direct convergence tests are reported in Sec. S4 of the Supplemental Material [24].

III. RESULTS AND DISCUSSION

A. Pure-component melting curves

The melting temperatures $T_m^0(P)$ of pure Al and pure Mg are first determined using the PCFC method, providing the pressure-dependent anchors for the Al-rich and Mg-rich limits of the binary Al-Mg alloy phase diagram, respectively.

1. Melting curve of fcc Al

Aluminium crystallises in the fcc structure at ambient conditions, with a melting point of 933 K [36]. Under compression, it undergoes structural transitions to hcp at ∼180 GPa and subsequently to bcc at ∼370 GPa [37–39], both well beyond the pressure range of interest. The fcc phase therefore governs the melting behaviour of Al throughout 0–150 GPa and is the only structure considered.

Two EAM reference potentials, $\mathrm{EAM}^{\mathrm{fcc}}_{\mathrm{low}}$ and $\mathrm{EAM}^{\mathrm{fcc}}_{\mathrm{high}}$, are trained at low and high pressure, respectively; their optimized parameters are listed in Table I (see Sec. S1 of the Supplemental Material [24] for details). Using these potentials, large-scale coexistence simulations are performed on a $10 \times 10 \times 20$ supercell of 8000 fcc Al atoms, evolved in the NVE ensemble for 300 ps with a 1 fs time step, confirmed by an energy drift test to be below 0.04 K/ps. Free-energy corrections are then computed from canonical-ensemble MD simulations on 500-atom fcc supercells for both solid and liquid phases at each reference melting point, run for 300 ps with a 1 fs timestep. A total of 100 statistically independent configurations are extracted by sampling every 1000 fs and subjected to DFT single-point calculations on a $2 \times 2 \times 2$ k-point grid.

TABLE I. Optimized EAM parameters for all reference potentials used in this work. For each element and phase, low- and high-pressure potentials are listed. n and m: repulsive and attractive exponents; ϵ: energy scale (eV); a: length scale (Å); C: dimensionless scaling factor.

System	Potential	n	m	ϵ	a	C
Al (fcc)	$\mathrm{EAM}^{\mathrm{fcc}}_{\mathrm{low}}$	6.9025	3.6265	0.1558	3.2523	9.9562
	$\mathrm{EAM}^{\mathrm{fcc}}_{\mathrm{high}}$	6.4638	2.7634	0.2663	3.0441	10.2388
Mg (hcp)	$\mathrm{EAM}^{\mathrm{hcp}}_{\mathrm{low}}$	7.680	4.105	0.0950	3.604	11.918
	$\mathrm{EAM}^{\mathrm{hcp}}_{\mathrm{high}}$	7.965	5.892	0.0150	3.919	11.449
Mg (bcc)	$\mathrm{EAM}^{\mathrm{bcc}}_{\mathrm{low}}$	8.475	5.734	0.0666	3.489	11.906
	$\mathrm{EAM}^{\mathrm{bcc}}_{\mathrm{high}}$	8.529	5.909	0.0111	3.875	11.497

The EAM reference melting temperatures and perturbatively corrected *ab initio* results are shown in Fig. 2(a). For $\mathrm{EAM}^{\mathrm{fcc}}_{\mathrm{low}}$, corrections ΔT are small at low pressure but grow increasingly as the potential moves outside its training regime at high pressure. $\mathrm{EAM}^{\mathrm{fcc}}_{\mathrm{high}}$ shows the complementary behavior: Corrections are largest at low pressure and decrease steadily, becoming negligibly small at high pressure where the potential was parametrized. Despite starting from very different reference potentials, the two independently corrected *ab initio* melting curves converge to a mutually consistent result over their common pressure interval (∼26–115 GPa), providing a stringent internal validation of the perturbative framework. To avoid uncontrolled extrapolation outside the controlled phase-space overlap regime, a strict validity threshold of $|\Delta G^{ls}| \leqslant 25$ meV/atom is enforced across all potentials; state points exceeding this window are excluded from the final melting curve (see Sec. S2 and Figs. S3–S5 of the Supplemental Material [24] for running convergence and threshold diagnostics). The computed melting curve is in excellent agreement with experimental and theoretical results across the full pressure range [36,40–44], as shown in Fig. 2(d).

2. Melting curves of hcp and bcc Mg

Magnesium crystallises in the hcp structure at ambient conditions and undergoes a pressure-induced transition to bcc at ∼50 GPa at room temperature [45,46]. Since both solid phases are present within the pressure range of interest, their melting curves and the hcp–bcc phase boundary are established independently.

a. hcp–bcc phase boundary. The Gibbs free energy of each phase is computed within the quasiharmonic approximation using the finite-displacement method over a volume grid of 10.0–26.0 Å^3/atom (step 0.5 Å^3/atom) and temperatures of 1–6000 K (step 100 K). Electronic energies use $32 \times 32 \times 20$ and $28 \times 28 \times 28$ k-point meshes for hcp and bcc respectively. Phonon calculations employ $4 \times 4 \times 2$ (hcp) and $4 \times 4 \times 4$ (bcc) supercells, sampled with $7 \times 7 \times 4$ and $6 \times 6 \times 6$ k-point meshes respectively, with atomic displacements of 0.023 Å and a $12 \times 12 \times 12$ q-point grid for both

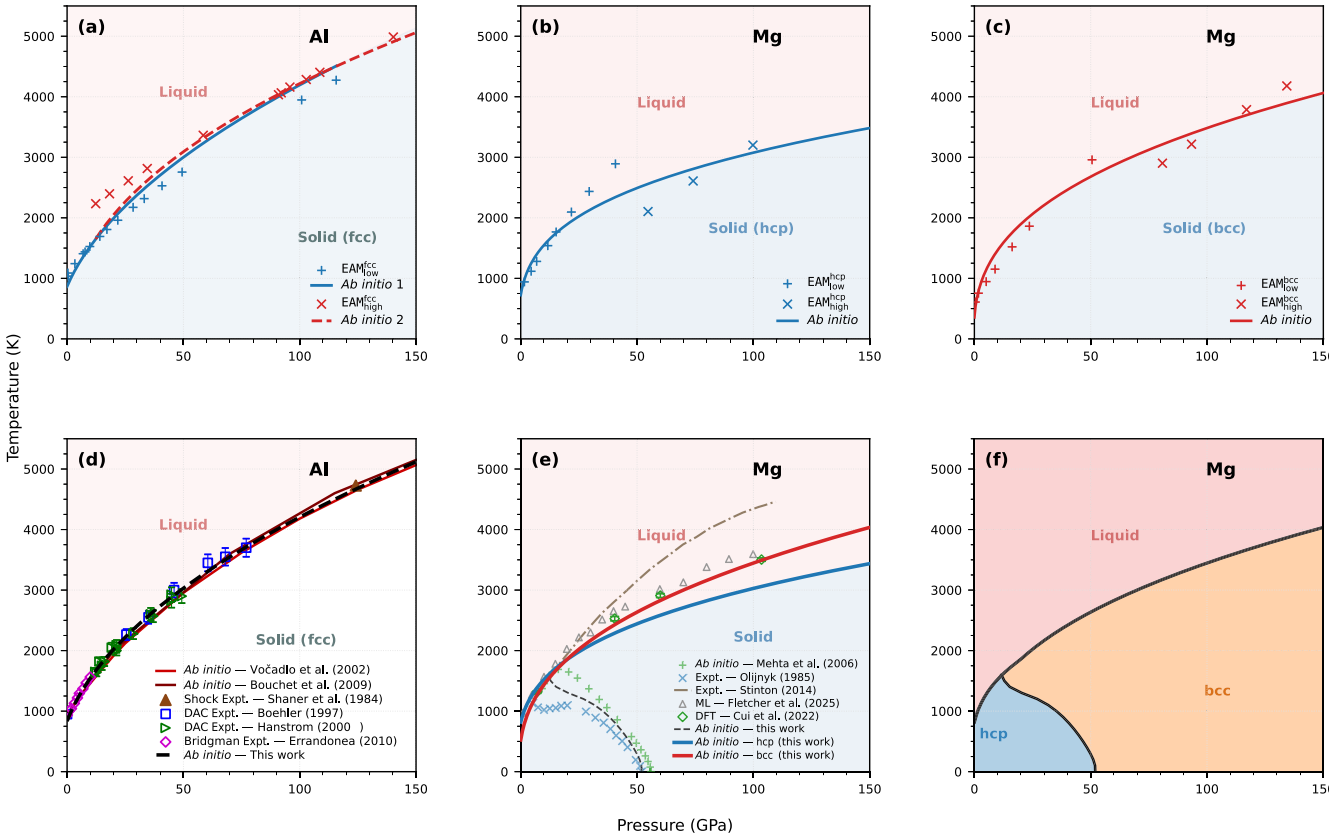


FIG. 2. *Ab initio* melting curves of fcc Al and Mg across 0–150 GPa. (a)–(c) EAM reference melting temperatures (symbols) and *ab initio* results (lines) for fcc Al, hcp Mg, and bcc Mg, respectively, using low- and high-pressure reference potentials. (d) Composite Al melting curve compared with prior *ab initio* calculations and experimental results. (e) Composite Mg melting curves for the hcp and bcc phases compared with experimental and theoretical results. (f) Computed Mg phase diagram showing the stability fields of hcp, bcc, and liquid phases and the hcp–bcc–liquid triple point.

phases. The phase boundary is located where the two Gibbs free energies are equal, as shown in Figs. 2(e)–2(f). The computed transition pressure at 300 K is 49.84 GPa, in excellent agreement with the experimental value of 50 ± 6 GPa [45] and the first-principles prediction of Mehta *et al.* [27]. The boundary carries a negative Clapeyron slope: The transition pressure decreases with increasing temperature, reflecting the higher vibrational entropy of the more open bcc structure, which becomes progressively stabilized relative to hcp under heating. Full phonon dispersion relations confirming that bcc Mg is dynamically stable throughout the phase-boundary regime ($P \geqslant 2$ GPa) are reported in Sec. S5 and Fig. S7 of the Supplemental Material [24].

b. hcp Mg melting curve. For the hcp phase, $\mathrm{EAM}_{\mathrm{low}}^{\mathrm{hcp}}$ is trained at low pressure and $\mathrm{EAM}_{\mathrm{high}}^{\mathrm{hcp}}$ at high pressure, providing complementary coverage of the hcp stability field; their parameters are listed in Table I. Coexistence simulations are performed on a $13 \times 13 \times 26$ supercell of 8788 Mg atoms, evolved in the NVE ensemble for 300 ps with a 1 fs time step. Free-energy corrections are obtained from canonical-ensemble MD simulations on 432-atom supercells, with 100 statistically independent configurations extracted by sampling every 1000 fs and evaluated with a $2 \times 2 \times 2$ k-point grid. The EAM reference melting temperatures and corrected *ab initio* hcp melting curve are shown in Fig. 2(b). Within each potential's fitted range, corrections ΔT are small; outside it, they grow systematically. The calculated hcp melting temperature at near-ambient pressure is 909 ± 13 K, in close agreement with the experimental value of 923 K.

c. bcc Mg melting curve. For the bcc phase, $\mathrm{EAM}_{\mathrm{low}}^{\mathrm{bcc}}$ is trained at intermediate pressure and $\mathrm{EAM}_{\mathrm{high}}^{\mathrm{bcc}}$ at high pressure, consistent with the bcc stability field; their parameters are listed in Table I. The coexistence simulations and free-energy corrections follow the same protocol as for the hcp phase: a $13 \times 13 \times 26$ supercell of 8788 Mg atoms evolved in the NVE ensemble for 300 ps with a 1 fs time step, with 432-atom supercells for the canonical MD corrections (run for 300 ps), 100 configurations sampled every 1000 fs, and a $2 \times 2 \times 2$ k-point grid for the DFT single-point evaluations. The EAM reference melting temperatures and corrected *ab initio* bcc melting curve are shown in Fig. 2(c). The bcc phase melts at only 605 ± 10 K near ambient pressure, well below the hcp value, reflecting the mechanical instability of the open bcc lattice at low compression. With increasing pressure, the bcc melting curve rises more steeply than the hcp branch and eventually surpasses it, consistent with the progressive entropic stabilisation of bcc under compression. Numerical thermodynamic parameters across representative state points of fcc Al, hcp Mg, and bcc Mg are tabulated in Sec. S3 (Tables S2 and S3) of the Supplemental Material [24].

d. Calculated Mg phase diagram. The full Mg phase diagram with distinct phase fields, assembling the hcp and bcc melting curves with the hcp–bcc phase boundary, is presented in Figs. 2(e) and 2(f). The hcp–bcc–liquid triple point is located at approximately $P^{\mathrm{TP}} = 11.7\,\mathrm{GPa}$ and $T^{\mathrm{TP}} = 1593\,\mathrm{K}$. As shown in Fig. 2(f), below the triple point hcp Mg occupies a compact stability field bounded above by its melting curve and to the right by the negatively sloped hcp–bcc boundary; above it, bcc dominates the entire high-pressure solid region up to 150 GPa. The liquid field covers the high-temperature domain above both melting curves, with the solid-to-liquid transition occurring via hcp below the triple point and via bcc above it. The computed phase boundaries agree well with available experimental and theoretical data [27,45–48].

B. Al–Mg phase diagram in the dilute-solute limit

With the *ab initio* melting curves of pure Al and Mg and the Mg hcp–bcc phase boundary established, the CPDS method is applied to compute the solidus and liquidus in the dilute-solute limit across 0–150 GPa, covering up to 6 at.% Mg on the Al-rich side and up to 6 at.% Al on the Mg-rich side.

1. Configuration sampling

On the Al-rich side, AIMD simulations are performed on 108-atom ($3 \times 3 \times 3$ fcc) supercells in the NVT ensemble at four pressures along the *ab initio* Al melting curve: 0, 54, 100, and 149 GPa, at the corresponding melting temperatures of 930, 3204, 4277, and 5056 K. On the Mg-rich side, hcp supercells ($5 \times 5 \times 5$, 250 atoms) are used at 0 GPa and bcc supercells ($6 \times 6 \times 6$, 216 atoms) at 60, 90, and 150 GPa, consistent with the calculated hcp–bcc phase boundary, at the corresponding *ab initio* Mg melting temperatures of 920, 2823, 3306, and 4037 K. Canonical AIMD trajectories are propagated using a $2 \times 2 \times 2$ Monkhorst–Pack k-point grid. Following a ∼5 ps equilibration period, production trajectories of ∼30 ps are sampled at 50 fs intervals, with structural correlation times $\tau \approx 50$ fs. In both cases, independent trajectories are generated for the pure solvent ($\lambda = 0$) and the single-solute-substituted system ($\lambda = 1$) in both solid and liquid phases. Standard errors on $\Delta\mu_X^{ls}$ are obtained from the endpoint sample statistics and propagated through the two-endpoint estimator. The thermodynamic inputs extracted from the AIMD trajectories are summarised in Table II. For Al, $\Delta V = V^l - V^s$ decreases from 1.29 Å^3/atom at 0 GPa to 0.19 Å^3/atom at 149 GPa (a factor of ∼7), and Δs^0_{Al} decreases smoothly from 1.30 to 0.88 k_{B}/atom, reflecting the progressive structural convergence of solid and liquid under compression. For Mg, the compression of ΔV is far more pronounced, from 1.15 to 0.06 Å^3/atom (a factor of ∼19), consistent with the considerably higher compressibility of Mg relative to Al. Notably, Δs^0_{Mg} exhibits a near-plateau between 60 and 90 GPa (0.82 to 0.81 k_{B}/atom), departing from the otherwise smooth monotonic decrease. This coincides with the bcc stability field: the more open and less ordered bcc lattice is structurally closer to the liquid than hcp, partially offsetting the compression-driven convergence of the two phases.

The trajectory diagnostics for both limits are shown in Fig. 3. In both cases, the energy traces for $\lambda = 0$ and $\lambda = 1$ fluctuate about well-defined stationary means with no systematic drift, confirming stable NVT sampling throughout. The mean-square displacement (MSD) curves confirm phase identity at all pressures: Solid trajectories plateau rapidly to ∼0.2 Å^2, while liquid trajectories grow linearly, confirming sustained diffusion. The MSD curves for $\lambda = 0$ and $\lambda = 1$ are nearly indistinguishable in both phases at all pressures, confirming that the single solute substitution does not structurally or dynamically perturb the host, consistent with the weak-perturbation requirement of the thermodynamic integration scheme.

A physically important contrast between the two limits is already visible at this stage. On the Al-rich side [Figs. 3(a)–3(d)], the $\lambda = 1$ energy lies consistently above $\lambda = 0$ in both phases at all pressures, indicating that substituting Mg into Al raises the total energy. On the Mg-rich side [Figs. 3(e)–3(h)], the ordering is reversed: $\lambda = 1$ lies consistently below $\lambda = 0$, reflecting the stronger bonding of Al relative to Mg in the Mg host. This reversed energy offset is the direct microscopic precursor of the partitioning reversal on the Mg-rich side, as quantified in the following section.

TABLE II. Thermodynamic properties of the equilibrated solid and liquid phases along the *ab initio* melting curve, obtained from the AIMD trajectories used in the thermodynamic integration, compared with DFT and experimental reference benchmarks at ambient pressure. For Mg, the solid phase is hcp at 0 GPa and bcc at 60–150 GPa. All volumes in Å^3/atom; $\Delta V = V^l - V^s$; Δs^0_A in k_{B}/atom. All compared literature quantities are defined identically to those calculated in the present work.

System/source	P (GPa)	T (K)	V^s	V^l	ΔV	Δs^0_A
Al (this work)	0	930	17.78	19.07	1.29	1.30
DFT [36]	0	912	17.70		1.51	1.35
Expt. [49,50]	0	933			1.24	1.38
Al	54	3204	12.63	13.03	0.40	0.97
Al	100	4277	10.94	11.20	0.26	0.92
Al	149	5056	9.82	10.02	0.19	0.88
Mg (this work)	0	920	24.76	25.91	1.15	0.99
DFT [51]	0	890	24.30	25.40	1.10	
Expt. [52,53]	0	923	24.65	25.38	0.76	1.11
Mg	60	2823	13.52	13.71	0.20	0.82
Mg	90	3306	11.99	12.13	0.13	0.81
Mg	150	4037	10.18	10.24	0.06	0.77

2. Chemical potential estimation

The validity of the two-endpoint perturbative scheme is first assessed through the TI integrand $\langle \Delta U \rangle_\lambda - \bar{U}$, shown as a function of λ for both compositional limits in Fig. 4. Subtracting the simple average $\bar{U}$ centers the ordinate so a perfectly linear integrand appears as two coincident lines passing through zero; any departure from zero directly measures nonlinearity. In both limits, in both phases, and at all pressures, the blue ($\lambda = 0$) and orange ($\lambda = 1$) linear approximations are in close mutual agreement, the $\pm 1\sigma$ uncertainty corridor between them is extremely narrow, and the fluctuation widths $\sqrt{\langle \delta \Delta U^2 \rangle}$ are small. This confirms that both the Al → Mg and Mg → Al transmutations constitute weak perturbations and that $\langle \Delta U \rangle_\lambda$ is well approximated

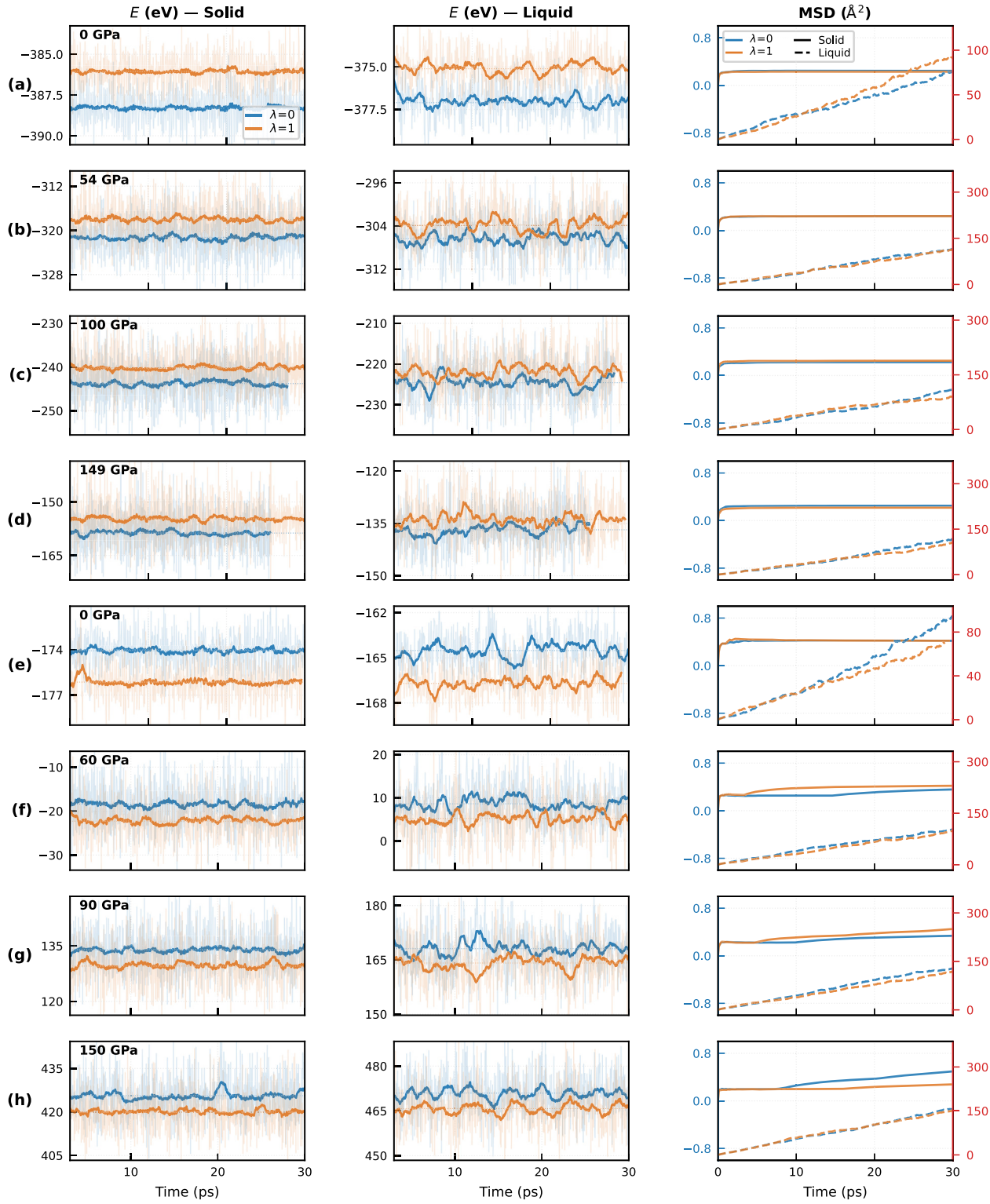


FIG. 3. AIMD trajectory diagnostics at each pressure. Rows (a)–(d) Al-rich limit (Mg solute in Al) at 0, 54, 100, and 149 GPa. Rows (e)–(h): Mg-rich limit (Al solute in Mg) at 0, 60, 90, and 150 GPa. Each row shows the instantaneous energy for $\lambda = 0$ (blue) and $\lambda = 1$ (orange) in the solid (left) and liquid (center) phases, with rolling averages as thick lines; the right panel shows the MSD for solid (blue, left axis) and liquid (red, right axis), with solid and dashed lines for $\lambda = 0$ and $\lambda = 1$, respectively. In rows (a)–(d), the $\lambda = 1$ energy lies consistently above $\lambda = 0$; in rows (e)–(h) the ordering is reversed, reflecting the stronger bonding of Al in the Mg host.

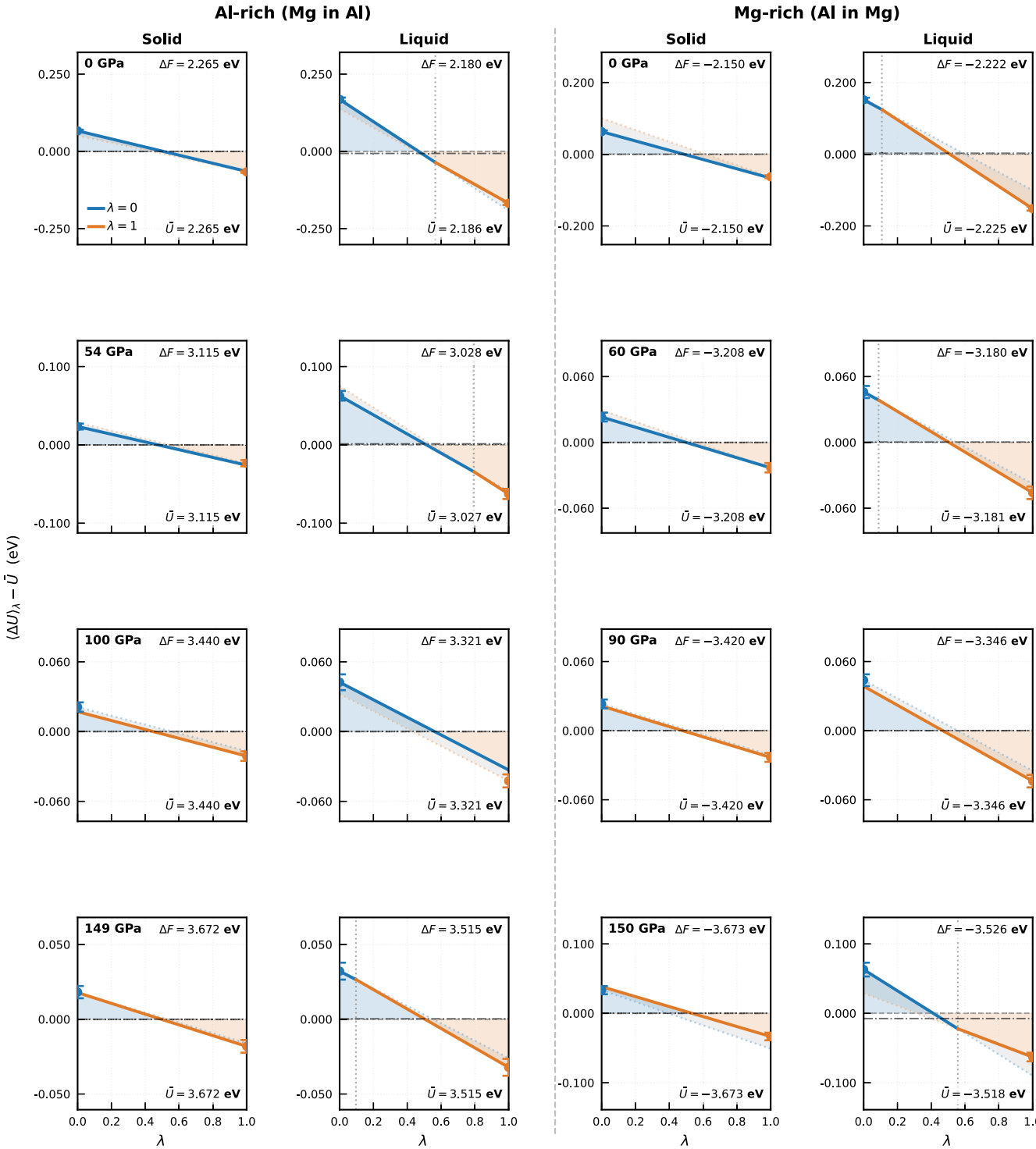


FIG. 4. Perturbative TI integrand $\langle \Delta U \rangle_\lambda - \bar{U}$ as a function of λ for the Al-rich limit (Mg solute in Al, left two columns) and the Mg-rich limit (Al solute in Mg, right two columns), each showing solid and liquid phases at four pressures (rows). Subtracting $\bar{U}$ centers the ordinate so deviations from zero directly quantify nonlinearity. Blue and orange lines show the linear approximations anchored at $\lambda = 0$ and $\lambda = 1$, respectively; shaded bands give the $\pm 1\sigma$ uncertainty corridor.

as linear across [0,1], validating the two-endpoint integration scheme throughout. This mutual agreement between the forward and backward endpoint expansions provides an internal consistency verification of path linearity across $\lambda \in [0, 1]$, confirming the robustness of the two-endpoint scheme without requiring intermediate coupling states.

The colored fills provide an additional visual indicator of which estimator is applied. Where the two linear approximations do not intersect within [0,1], the blue and orange fills are approximately equal in area and opposite in sign, confirming that the correction to $\bar{U}$ is negligible and the simple-average estimator is adopted. Where the approximations cross at an

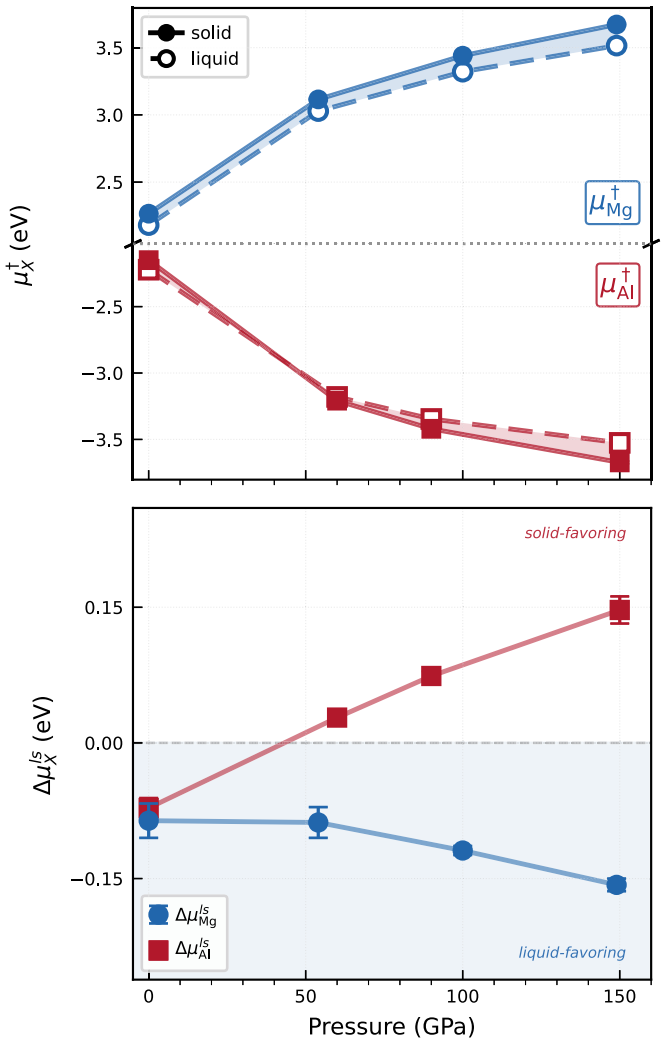


FIG. 5. Pressure evolution of the excess chemical potentials and their difference for Mg in Al (blue) and Al in Mg (red). Upper panel: Individual solid ($\mu_X^{\dagger s}$, filled symbols) and liquid ($\mu_X^{\dagger l}$, open symbols) excess chemical potentials; the shaded band between each solid–liquid pair highlights the sign and magnitude of the partitioning tendency. Lower panel: Excess chemical potential difference $\Delta\mu_X^{ls} = \mu_X^{\dagger l} - \mu_X^{\dagger s}$, with blue shading indicating the liquid-favoring regime ($\Delta\mu_X^{ls} < 0$) and red shading indicating the solid-favoring regime ($\Delta\mu_X^{ls} > 0$).

interior point $\lambda^* \in (0, 1)$, the fills are unequal and encode a nonzero signed correction, so the piecewise-linear estimator is applied instead. In all cases, the correction beyond $\bar{U}$ is small, confirming that the perturbative assumption is well satisfied across both limits and all pressures.

The resulting excess chemical potentials are shown in Fig. 5. The upper panel reveals a striking mirror symmetry between the two limits: $\mu_{Mg}^{\dagger s}$ and $\mu_{Mg}^{\dagger l}$ are both positive and rise monotonically with pressure, while $\mu_{Al}^{\dagger s}$ and $\mu_{Al}^{\dagger l}$ are both negative and decrease monotonically, with comparable magnitudes across the full pressure range. This near-antisymmetry reflects the close chemical affinity of Al and Mg as neighboring elements: substituting Mg into Al costs energy, raising the excess chemical potential above zero, while substituting Al into Mg releases energy by a similar amount, driving it below zero. The shaded band between each solid–liquid pair encodes the partitioning tendency: a narrow band indicates weak fractionation, while a wide band indicates strong partitioning. On the Al-rich side, the solid value of $\mu_{Mg}^{\dagger}$ lies consistently above the liquid value at all pressures, and the gap between them widens progressively with compression. On the Mg-rich side, the two values converge with increasing pressure and reverse their ordering such that the solid lies below the liquid by 60 GPa.

Despite the overall mirror symmetry in magnitude, it is precisely this reversal in the solid–liquid ordering on the Mg-rich side that breaks the symmetry between the two limits. The lower panel of Fig. 5 makes this explicit by showing $\Delta\mu_X^{ls} = \mu_X^{\dagger l} - \mu_X^{\dagger s}$ directly, with blue shading for liquid favoring ($\Delta\mu_X^{ls} < 0$) and red shading for solid favoring ($\Delta\mu_X^{ls} > 0$) regimes. On the Al-rich side, $\Delta\mu_{Mg}^{ls}$ grows monotonically more negative with pressure, reflecting a continuously strengthening liquid favoring preference for Mg with no sign of reversal across the full pressure range. On the Mg-rich side, $\Delta\mu_{Al}^{ls}$ begins negative at ambient pressure and is explicitly confirmed to be solid-favouring at the first calculated bcc point of 60 GPa ($\Delta\mu_{Al}^{ls} = +28 \pm 6$ meV, $k = 1.12 \pm 0.03$), growing steadily positive thereafter without saturation. This sign reversal signals a complete change in the direction of Al partitioning under compression, occurring within the bcc stability field of the Mg host (above the 11.7 GPa triple point), and directly produces the topological inversion of the Mg-rich phase diagram discussed in the following section.

3. Phase diagram

With $T_m^0(P)$, $\Delta\mu_X^{ls}(P)$, and $\Delta s_A^0(P)$ established, the solidus and liquidus at both compositional extremes are constructed by solving the dilute-solution phase-equilibrium relations [Eqs. (6) and (7)] self-consistently at each pressure, representing dilute-limit extrapolations where solute–solute interactions are neglected.

On the Al-rich side, the resulting phase diagrams are shown in the top row of Fig. 6. At ambient pressure, the computed solidus and liquidus reproduce the experimental data of Murray [22] closely across the full 0–6 at. % Mg range, providing direct validation of the framework. The partition coefficient $k = 0.35 \pm 0.08$ indicates that the solid retains only about one-third of the Mg present in the coexisting liquid, producing a correspondingly wide coexistence field. As pressure increases to 54 GPa, k rises sharply to 0.74 ± 0.04 and the coexistence width narrows substantially. This narrowing is driven primarily by the reduction in Δs_{Al}^0 from $1.30\,k_B$/atom at ambient to $0.97\,k_B$/atom at 54 GPa: as the entropy of fusion decreases, the liquidus and solidus slopes steepen and converge, compressing the two-phase field even as $|\Delta\mu_{Mg}^{ls}|$ grows. At 100 and 149 GPa, k stabilizes near 0.73 ± 0.01 and 0.70 ± 0.01, respectively, indicating that the competing effects of a growing $|\Delta\mu_{Mg}^{ls}|$ and a declining Δs_{Al}^0 increasingly balance, driving k toward a high-pressure asymptote. The overall topology is preserved throughout: both boundaries slope negatively with Mg concentration and Mg consistently favors the liquid across the full pressure range.

On the Mg-rich side, shown in the bottom row of Fig. 6, the pressure evolution is qualitatively richer. At ambient

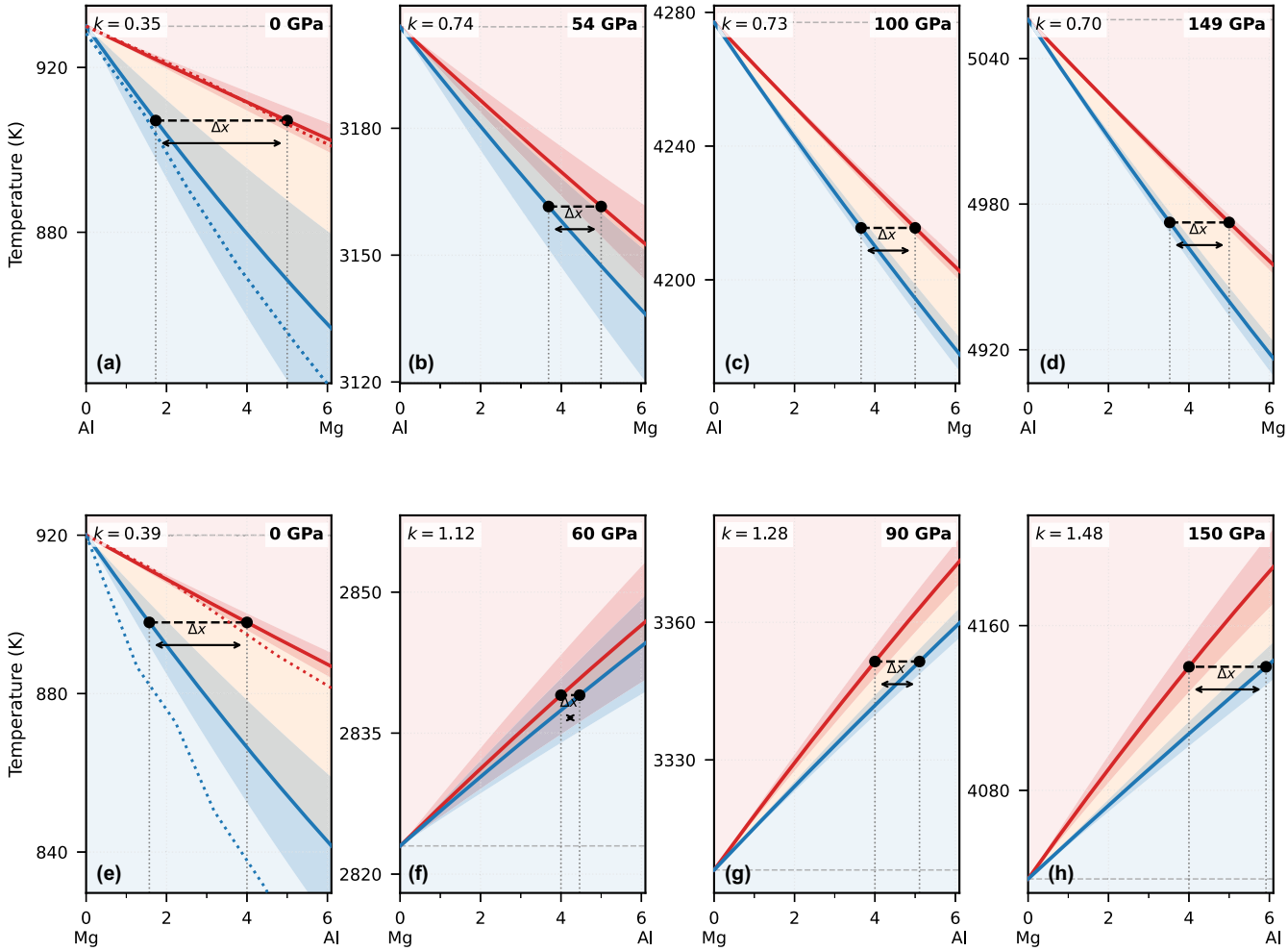


FIG. 6. *Ab initio* Al–Mg dilute-solute phase diagrams (first-order dilute extrapolations). Top row (a)–(d): Al-rich limit (Mg solute in Al) at 0, 54, 100, and 149 GPa. Bottom row (e)–(h): Mg-rich limit (Al solute in Mg) at 0, 60, 90, and 150 GPa. Liquidus (red curve and red $\pm 1\sigma$ band) and solidus (blue curve and blue $\pm 1\sigma$ band) delimit the single-phase liquid (light-red fill), single-phase solid (light-blue fill), and two-phase coexistence (orange fill) regions, with darker shading arising where $\pm 1\sigma$ uncertainty bands overlap. Representative tie lines at $x_{\mathrm{Mg}} = 5\%$ (top) and $x_{\mathrm{Al}} = 4\%$ (bottom) illustrate $k = c_s/c_l$ and the coexistence width Δx.

pressure, the framework reproduces the experimental data of Murray [22] closely, with $k = 0.39 \pm 0.06$ and the liquidus slope agreeing to within ∼6%, validating the approach on the Mg-rich side. At 60 GPa, the sign reversal in $\Delta\mu^{ls}_{\mathrm{Al}}$ has already taken full effect: the topology of the diagram inverts, with both boundaries now sloping positively with Al concentration and k rising to 1.12 ± 0.03 (confirming $k > 1$). The solid now incorporates more Al than the coexisting liquid, and the melting temperature increases with Al addition rather than decreasing. The coexistence field is relatively narrow at 60 GPa, reflecting the modest magnitude of $\Delta\mu^{ls}_{\mathrm{Al}}$ just above the reversal pressure combined with the reduced $\Delta s^{0}_{\mathrm{Mg}}$. At 90 GPa, solid-favouring partitioning is more firmly established with $k = 1.28 \pm 0.02$, and the coexistence field begins to re-broaden as the growing magnitude of $\Delta\mu^{ls}_{\mathrm{Al}}$ increasingly offsets the entropy-driven narrowing. By 150 GPa, the reversal is fully developed: $k = 1.48 \pm 0.07$ and the coexistence field has re-broadened substantially. Unlike the Al-rich side where k saturates, k on the Mg-rich side increases monotonically across the studied pressure range up to 150 GPa without exhibiting saturation, reflecting the continuously strengthening structural preference of Al for the bcc solid.

The two limits together reveal a fundamental asymmetry in how solute partitioning evolves under extreme compression: on the Al-rich side, the liquid-favoring preference of Mg strengthens monotonically and saturates at high pressure, consistent with the persistent atomic volume disparity between the larger Mg solute and the increasingly compressed Al host lattice; on the Mg-rich side, the partitioning of Al undergoes a complete reversal within the bcc stability field of the host, where Al progressively favours the solid over the liquid under compression. This partitioning reversal, absent on the Al-rich side where the fcc host remains stable throughout, is what distinguishes the two limits fundamentally and makes the Mg-rich phase diagram qualitatively richer under compression. We emphasize that while the close agreement with the Murray phase diagram at ambient pressure validates our computational framework in the low-pressure dilute regime, direct experimental phase-boundary or partitioning measurements

for the Al–Mg binary alloy at high pressure are currently unavailable. The high-pressure phase boundaries plotted up to 6 at. % represent first-order dilute-limit extrapolations, and the predicted partitioning reversal ($k > 1$) constitutes a theoretical prediction that awaits experimental validation.

IV. CONCLUSION

We have applied a fully *ab initio* framework to compute the dilute-limit phase diagram of the Al–Mg binary system from ambient conditions up to 150 GPa, establishing melting curves for pure fcc Al and hcp/bcc Mg, the Mg hcp–bcc phase boundary and triple point, and the solidus, liquidus, and solute partition coefficient at both compositional extremes.

The *ab initio* melting curves of both metals agree closely with available experimental and theoretical data across the full pressure range, validating the PCFC approach in two structurally distinct systems. For Mg, the hcp–bcc transition requires independent treatment of the two structural branches; the composite melting curve is thermodynamically continuous across the transition and the computed triple point is in reasonable agreement with experimental estimates.

On the Al-rich side, Mg consistently favors the liquid throughout 0–150 GPa, with the liquid-favouring preference strengthening monotonically under compression and the partition coefficient approaching a high-pressure asymptote within the studied pressure range. The computed phase boundaries reproduce the experimental data of Murray [22] closely at ambient pressure, validating the framework on this side.

On the Mg-rich side, Al partitions into the liquid at ambient pressure but undergoes a complete pressure-driven reversal within the bcc stability field of the Mg host, becoming solid-favouring by 60 GPa ($k = 1.12 \pm 0.03$). The partition coefficient crosses unity in this pressure interval and continues to rise across the studied pressure range up to 150 GPa without exhibiting saturation. This reversal inverts the topology of the Mg-rich coexistence field from a conventional downward-sloping to an upward-sloping phase boundary, a feature with no counterpart on the Al-rich side. Together, the two limits reveal a fundamental thermodynamic asymmetry under compression associated with the stability of the high-pressure bcc phase of the Mg host.

While a metallic Al–Mg binary does not directly represent complex multicomponent silicate or oxide mantles, it serves as a valuable model system demonstrating that high-pressure partitioning can deviate qualitatively from low-pressure behavior, and the first-principles methodology developed here is transferable to planetary partitioning problems. The pressure-driven reversal of Al partitioning (becoming solid-favouring by 60 GPa) illustrates that in deep Mg-rich metallic or planetary systems, solute elements can be preferentially incorporated into the growing solid during progressive crystallisation rather than expelled into the residual melt, contrary to ambient-pressure expectations. Because direct experimental binary partitioning data under extreme compression are presently lacking, these findings serve as *ab initio* predictions that await experimental validation.

ACKNOWLEDGMENTS

We acknowledge the support of AWE Nuclear Security Technologies and the HPC facility at UCL. This work also used the ARCHER2 UK National Supercomputing Service [54] under the Mineral Consortium allocation.

S.B.S.: Investigation (equal) and writing—original draft (equal). S.M.: Funding acquisition (supporting). D.A.: Supervision (equal).

The authors have no conflicts to disclose.

DATA AVAILABILITY

The data that support the findings of this study are available from the corresponding author upon reasonable request.

[1] D. R. Gaskell and D. E. Laughlin, *Introduction to the Thermodynamics of Materials* (CRC Press, Boca Raton, FL, 2024).

[2] *ASM Handbook, Vol. 3: Alloy Phase Diagrams*, edited by H. Okamoto, M. E. Schlesinger, and E. M. Mueller (ASM International, Materials Park, OH, 2016).

[3] J. Schön and M. Jansen, Prediction, determination and validation of phase diagrams via the global study of energy landscapes, Int. J. Mater. Res. **100**, 135 (2009).

[4] M. Enoki, S. Minamoto, I. Ohnuma, T. Abe, and H. Ohtani, Current status and future scope of phase diagram studies, ISIJ International **63**, 407 (2023).

[5] *Phase Diagrams: Understanding the Basics,* edited by F. C. Campbell (ASM International, Materials Park, OH, 2012).

[6] *Methods for Phase Diagram Determination*, edited by J.-C. Zhao (Elsevier, Oxford, 2007).

[7] H. Lukas, S. G. Fries, and B. Sundman, *Computational Thermodynamics: The CALPHAD Method* (Cambridge University Press, Cambridge, UK, 2007).

[8] N. Saunders and A. P. Miodownik, *CALPHAD (Calculation of Phase Diagrams): A Comprehensive Guide*, Pergamon Materials Series Vol. 1 (Pergamon, Oxford, 1998).

[9] F. Zipoli, V. Viterbo, O. Schilter, L. Kahle, and T. Laino, Prediction of phase diagrams and associated phase structural properties, Ind. Eng. Chem. Res. **61**, 8378 (2022).

[10] G. Wang, C. Wang, X. Zhang, Z. Li, J. Zhou, and Z. Sun, Machine learning interatomic potential: Bridge the gap between small-scale models and realistic device-scale simulations, Iscience **27**, 109673 (2024).

[11] S. Zhu, D. Sarıtürk, and R. Arróyave, Machine learning potentials for alloys: A detailed workflow to predict phase diagrams and benchmark accuracy, npj Comput. Mater. **11**, 340 (2025).

[12] A. Walle and G. Ceder, Automating first-principles phase diagram calculations, J. Phase Equilibria **23**, 348 (2002).

[13] S. Liu, G. Esteban-Manzanares, and J. LLorca, First principles prediction of the Al-Li phase diagram, Metall. Mater. Trans. A **52**, 4675 (2021).

[14] D. Alfè, M. J. Gillan, and G. D. Price, *Ab initio* chemical potentials of solid and liquid solutions and the chemistry of the Earth's core, J. Chem. Phys. **116**, 7127 (2002).
[15] D. Alfè, M. J. Gillan, and G. D. Price, Composition and temperature of the Earth's core constrained by combining *ab initio* calculations and seismic data, Earth Planet. Sci. Lett. **195**, 91 (2002).
[16] J. Chipman, Thermodynamics and phase diagram of the Fe-C system, Metall. Trans. **3**, 55 (1972).
[17] K. Hirose, B. Wood, and L. Vočadlo, Light elements in the Earth's core, Nat. Rev. Earth Environ. **2**, 645 (2021).
[18] Z. Zhang, G. Csányi, D. Alfè, Y. Zhang, J. Li, and J. Liu, Free energies of Fe-O-Si ternary liquids at high temperatures and pressures: Implications for the evolution of the Earth's core composition, Geophys. Res. Lett. **49**, e2021GL096749 (2022).
[19] S. B. Sharma, S. Mehta, and D. Alfè, *Ab initio* phase diagrams of binary alloys in the low solute concentration limit, J. Chem. Phys. **162**, 184502 (2025).
[20] M. Mendelev, M. Asta, M. Rahman, and J. Hoyt, Development of interatomic potentials appropriate for simulation of solid–liquid interface properties in Al–Mg alloys, Philos. Mag. **89**, 3269 (2009).
[21] M. P. Liu, H. J. Roven, M. Y. Murashkin, R. Z. Valiev, A. Kilmametov, Z. Zhang, and Y. Yu, Structure and mechanical properties of nanostructured Al–Mg alloys processed by severe plastic deformation, J. Mater. Sci. **48**, 4681 (2013).
[22] J. L. Murray, The Al-Mg (aluminum-magnesium) system, J. Phase Equilib. **3**, 60 (1982).
[23] M. S. Daw and M. I. Baskes, Semiempirical, quantum mechanical calculation of hydrogen embrittlement in metals, Phys. Rev. Lett. **50**, 1285 (1983).
[24] See Supplemental Material at http://link.aps.org/supplemental/10.1103/q4q1-q4g8 for quantitative EAM benchmark errors and residual distributions, running free-energy convergence diagnostics and threshold tolerance, complete numerical thermodynamic parameters along the melting lines, supercell size and k-point discretization convergence tests, phonon dispersion relations and dynamical stability of Mg, and explicit analytical error propagation formulations.
[25] M. P. Allen and D. J. Tildesley, *Computer Simulation of Liquids* (Oxford University Press, Oxford, 2017).
[26] D. Alfè, M. J. Gillan, and G. D. Price, Complementary approaches to the *ab initio* calculation of melting properties, J. Chem. Phys. **116**, 6170 (2002).
[27] S. Mehta, G. D. Price, and D. Alfè, *Ab initio* thermodynamics and phase diagram of solid magnesium: A comparison of the LDA and GGA, J. Chem. Phys. **125**, 194507 (2006).
[28] D. Alfè, PHON: A program to calculate phonons using the small displacement method, Comput. Phys. Commun. **180**, 2622 (2009).
[29] G. Kresse and J. Furthmüller, Efficient iterative schemes for *ab initio* total-energy calculations using a plane-wave basis set, Phys. Rev. B **54**, 11169 (1996).
[30] G. Kresse and D. Joubert, From ultrasoft pseudopotentials to the projector augmented-wave method, Phys. Rev. B **59**, 1758 (1999).
[31] P. E. Blüochl, Projector augmented-wave method, Phys. Rev. B **50**, 17953 (1994).
[32] J. P. Perdew, K. Burke, and M. Ernzerhof, Generalized gradient approximation made simple, Phys. Rev. Lett. **77**, 3865 (1996).
[33] N. D. Mermin, Thermal properties of the inhomogeneous electron gas, Phys. Rev. **137**, A1441 (1965).
[34] S. Nosé, A molecular dynamics method for simulations in the canonical ensemble, Mol. Phys. **52**, 255 (1984).
[35] H. J. Monkhorst and J. D. Pack, Special points for Brillouin-zone integrations, Phys. Rev. B **13**, 5188 (1976).
[36] L. Vočadlo and D. Alfè, *Ab initio* melting curve of the fcc phase of aluminum, Phys. Rev. B **65**, 214105 (2002).
[37] D. N. Polsin, D. E. Fratanduono, J. R. Rygg, A. Lazicki, R. F. Smith, J. H. Eggert, M. C. Gregor, B. J. Henderson, X. Gong, J. A. Delettrez, R. G. Kraus, P. M. Celliers, F. Coppari, D. C. Swift, C. A. McCoy, C. T. Seagle, J.-P. Davis, S. J. Burns, G. W. Collins, and T. R. Boehly, X-ray diffraction of ramp-compressed aluminum to 475 GPa, Phys. Plasmas **25**, 082709 (2018).
[38] Y. Akahama, M. Nishimura, K. Kinoshita, H. Kawamura, and Y. Ohishi, Evidence of a fcc-hcp transition in aluminum at multimegabar pressure, Phys. Rev. Lett. **96**, 045505 (2006).
[39] Y. B. Kudasov, O. Surdin, A. Korshunov, V. Pavlov, N. Frolova, and R. Kuzin, Lattice dynamics and phase diagram of aluminum at high temperatures, J. Exp. Theor. Phys. **117**, 664 (2013).
[40] J. Bouchet, F. Bottin, G. Jomard, and G. Zérah, Melting curve of aluminum up to 300 GPa obtained through *ab initio* molecular dynamics simulations, Phys. Rev. B **80**, 094102 (2009).
[41] R. Boehler and M. Ross, Melting curve of aluminum in a diamond cell to 0.8 Mbar: Implications for iron, Earth Planet. Sci. Lett. **153**, 223 (1997).
[42] A. Hänström and P. Lazor, High pressure melting and equation of state of aluminium, J. Alloys Compd. **305**, 209 (2000).
[43] D. Errandonea, The melting curve of ten metals up to 12 GPa and 1600 K, J. Appl. Phys. **108**, 033517 (2010).
[44] *High Pressure in Science and Technology*, Proceedings of the 9th AIRAPT International High Pressure Conference, Albany, NY, 1983, Parts I-III, edited by C. Homan, R. K. MacCrone, and E. Whalley, Materials Research Society Symposia Proceedings Vol. 22 (North-Holland/Elsevier, New York, 1984).
[45] H. Olijnyk and W. Holzapfel, High-pressure structural phase transition in Mg, Phys. Rev. B **31**, 4682 (1985).
[46] G. W. Stinton, S. G. MacLeod, H. Cynn, D. Errandonea, W. J. Evans, J. E. Proctor, Y. Meng, and M. I. McMahon, Equation of state and high-pressure/high-temperature phase diagram of magnesium, Phys. Rev. B **90**, 134105 (2014).
[47] C. Cui, J. Xian, H. Liu, F. Tian, X. Gao, and H. Song, Melting curve of magnesium up to 460 GPa from *ab initio* molecular dynamics simulations, J. Appl. Phys. **131**, 195901 (2022).
[48] V. G. Fletcher, A. P. Bartók, and L. B. Pártay, Autonomous thermodynamically informed database generation for machine-learned interatomic potentials and application to magnesium, npj Comput. Mater. **12**, 36 (2026).
[49] J. E. Sansonetti and W. C. Martin, Handbook of basic atomic spectroscopic data, J. Phys. Chem. Ref. Data **34**, 1559 (2005).
[50] M. W. Chase Jr., C. A. Davies, J. R. Downey Jr., D. A. Frurip, R. A. McDonald, and A. N. Syverud, JANAF Thermochemical Tables, Third Edition, Part II: Cr–Zr, J. Phys. Chem. Ref. Data **14**(Suppl. 1), 927 (1985).

[51] Q.-J. Hong and A. van de Walle, Reentrant melting of sodium, magnesium, and aluminum: General trend, Phys. Rev. B **100**, 140102 (2019).

[52] J. F. Cannon, Behavior of the elements at high pressures, J. Phys. Chem. Ref. Data **3**, 781 (1974).

[53] M. W. Chase Jr., *NIST–JANAF Thermochemical Tables*, 4th ed., J. Phys. Chem. Ref. Data, Monograph 9 (American Chemical Society and American Institute of Physics, Woodbury, NY, 1998), pp. 1–1951.

[54] ARCHER2 (The UK National Supercomputing Service), https://www.archer2.ac.uk.